IEEE Open Journal of
Antennas and Propagation

Received 6 March 2022; accepted 12 March 2022. Date of publication 22 March 2022; date of current version 30 March 2022.

*Digital Object Identifier 10.1109/OJAP.2022.3161128*

# Frequency Selective Computational Through Wall Imaging Using a Dynamically Reconfigurable Metasurface Aperture

**THE VIET HOANG[1], RUPESH KUMAR[1], THOMAS FROMENTEZE[3], MARÍA GARCÍA-FERNÁNDEZ[1,2], GUILLERMO ÁLVAREZ-NARCIANDI[1,2], VINCENT FUSCO[1] (Fellow, IEEE), AND OKAN YURDUSEVEN[1] (Senior Member, IEEE)**

[1]Centre for Wireless Innovation, Institute of Electronics, Communications and Information Technology, Queen's University Belfast, Belfast BT3 9DT, U.K.

[2]Departamento de Ingeniería Eléctrica, Universidad de Oviedo, 33203 Gijón, Spain

[3]University of Limoges, XLIM, UMR 7252, 87000 Limoges, France

CORRESPONDING AUTHOR: O. YURDUSEVEN (e-mail: okan.yurduseven@qub.ac.uk)

This work was supported in part by the Leverhulme Trust through Research Leadership Award under Grant RL-2019-019, and in part by the Spanish Ministry of Universities and European Union (NextGenerationEU Fund) under Project MU-21-UP2021-030-71667225 and Project MU-21-UP2021-030-53519863.

**ABSTRACT** A two-dimensional (2D) dynamically reconfigurable metasurface aperture is presented to perform frequency selective through wall imaging (TWI) with an unknown structure of the wall. Generally, in TWI, the medium properties and thickness of the wall need to be known in advance, which is not always possible. Moreover, compensating for these effects can significantly increase the computational complexity. We propose a two-stage method that leverages the concept of a dynamically reconfigurable metasurface antenna (DMA) in a narrow frequency band in which the effects of the wall are minimum to perform TWI. First, two simple probe antennas are used to evaluate the reflection response of the wall by means of a simple backscatter measurement. Based on these characteristics, a narrow band frequency selective window is identified. Second, a DMA consisting of an array of tunable metamaterial elements is used for TWI in the identified frequency selective window. The DMA aperture enables the scene information to be sampled through a set of spatio-temporally varying quasi-random modes using a single-channel transmit and receive architecture. This physical-layer compression scheme can significantly simplify the data acquisition while the quasi-random sampling of the scene information eliminates the need for conventional raster-scan based modalities.

**INDEX TERMS** Reconfigurable antennas, microwave imaging, through wall imaging, metasurface.

## I. INTRODUCTION

THROUGH wall imaging (TWI) has become a promising way to detect and recognize various objects in a plethora of applications, such as rescue operations, surveillance, and reconnaissance [1]–[4]. Despite the capability of electromagnetic (EM) waves at microwave frequencies to see through optically opaque materials, to minimize distortions in the reconstructed images, imaging through a wall structure requires that the electrical and physical characteristics of the wall are known as a-priori information. In practical applications, this not only can be unfeasible, but also, accounting for the effects of the wall structure can be a computationally expensive process [5], [6]. Furthermore, in many practical scenarios, both the object to be imaged and the structure of the wall are unknown. Unfortunately, in that case, the wall contributes to increasing the clutter level of the measurements. The reason is that it may no longer be possible to separate the wall contributions from those beyond this structure.

Recently, active computational imaging techniques have received significant attention [7]–[9]. These techniques allow backscattered signals to be encoded into a series of indirect measurements through the use of quasi-random, spatio-temporally incoherent radiation patterns synthesized

from metasurface-based antennas. In contrast to conventional multi-pixel raster scan-based imaging systems, such as synthetic aperture radar (SAR) [10], [11] and phased arrays [12], [13], the computational imaging modality relies on probing the scene information using spatio-temporally incoherent modes and compressing the backscattered data into a single channel. Therefore, it can substantially improve the data acquisition speed and reduce the complexity of the hardware layer [14].

Frequency-diversity and dynamic apertures are two modalities that can be leveraged to create an ensemble of quasi-random sensing fields with spatial diversity [14]. In the frequency-diverse approach, the radiated fields from the aperture are governed by a frequency sweep with each frequency radiating a different radiation pattern. This can be achieved by various structures of metasurfaces, such as a parallel plate waveguide with metamaterial elements and mode-mixing cavities [15]–[30]. However, frequency-diverse apertures pose several drawbacks, such as the necessity to sweep a rather large bandwidth to synthesize a sufficient number of measurement modes, the extra complexity of the design of the radiofrequency (RF) hardware due to the large bandwidth requirements for imaging, and possible frequency interferences due to the microwave spectrum congestion.

Alternatively, it is possible to take advantage of dynamically modulated metasurface apertures to synthesize the quasi-random radiation patterns. Using dynamically modulated apertures, the radiation of spatio-temporally varying modes is achieved by electronically tuning the radiating metamaterial elements on the aperture over a narrow operating bandwidth or even at a single frequency [31]–[38]. As the generation of spatio-temporally varying modes only requires a narrow frequency band (or even just a single frequency), the dynamic modulation approach can rely on a substantially simplified RF backend architecture in comparison to the frequency-diversity approach. In this context, a preliminary study on computational TWI using a dynamic metasurface antenna (DMA) was presented in [37]. However, the work presented in [37] exhibits several limitations, such as (*i*) the structure of the wall needs to be known, which is not practical, (*ii*) compensation for the effects of the wall needs to be carried out using layered Green's functions, significantly increasing the computational complexity, and (*iii*) the use of one-dimensional (1D) metasurface limits the imaging field-of-view (FoV) only to a single axis in the transverse plane.

In this paper, leveraging two-port, two-dimensional (2D) DMAs operating over a narrow frequency bandwidth, computational TWI is presented with no a-priori knowledge of the wall structure. First, two probes are used to evaluate the EM response of the wall in a range of frequencies. Based on these characteristics, a narrow frequency band, called "frequency selective window" or "transmission window", is chosen to maximize the transmission through the wall. Next, a DMA including an array of sparsely distributed, tunable metamaterial elements is used to achieve TWI within the selected frequency window. To reconfigure the metasurface aperture, the metamaterial elements are integrated with PIN diodes that are reconfigured in a binary fashion (*on* or *off*). By tuning the states of the diodes randomly, the dynamic manipulation of the radiated fields is realized. TWI is then computed in the near-field region by leveraging the dynamically radiated characteristic of the DMA with no a-priori knowledge of the wall composition and structure, and without the additional need to compensate for the effects of the wall in the signal-processing layer.

This work is the first to demonstrate a computational DMA imaging concept for TWI without the need for a-priori knowledge of the imaging medium. Moreover, in comparison to [37], we achieve a 2D FoV in the transverse plane for TWI, which is a significant step forward compared with the 1D metasurface concept limited to single-axis TWI in the transverse plane. In addition, this work differs from [38] in two major ways. First, whereas the imaging scenario studied in [38] is only valid for free-space applications, the presented technique in this work can handle dielectric media. Second, whereas the major contribution of [38] is the DMA design, the focus of this work is not the antenna design, but rather the computational TWI technique achieved using a sensor fusion scheme to realize, *simultaneously*, (*i*) physical layer compression for single-pixel TWI and (*ii*) eliminating the need for layered Green's functions for TWI.

## II. DETERMINATION OF THE FREQUENCY SELECTIVE WINDOW

First, we will investigate the EM characteristics of the wall, including reflectance, transmittance and absorbance responses, when an incident wave illuminates and interacts with the wall. In this work, as the wall structure, we use a Terrace stone wall ($\varepsilon_r = 7.9$, $\tan\delta = 0.15$) [39] and note that different types of materials can also be chosen without loss of generality. For the presented TWI concept, K-band frequencies are considered. Fig. 1(a) shows a simple unit cell formed by a Terrace stone medium with a thickness of $t$ and a width of $\lambda_0/2$, where $\lambda_0$ is the free-space wavelength. Here, the incident wave is a plane wave with an incident angle of 0°. Figs. 1(b)-(d) show the transmittance, reflectance and absorbance of the wall, respectively, as a function of frequency and wall thickness. It is observed that when the thickness of the wall increases, a growing number of oscillations in the transmittance, reflectance and absorbance spectra appears across the studied frequency range, and vice versa. Further analyzing the results in Figs. 1(b)-(d), it is possible to choose certain sub-bands in the frequency range of 18–24 GHz. In this work, we assume that the thickness of the wall is 15 mm. Without having this information as a-priori, one can perform a frequency analysis to find an ideal sub-band in which the reflection from the wall is minimized, offering a maximized transmission through the wall. In other words, by doing a simple measurement of the wall structure, it is possible to identify an ideal frequency-band of

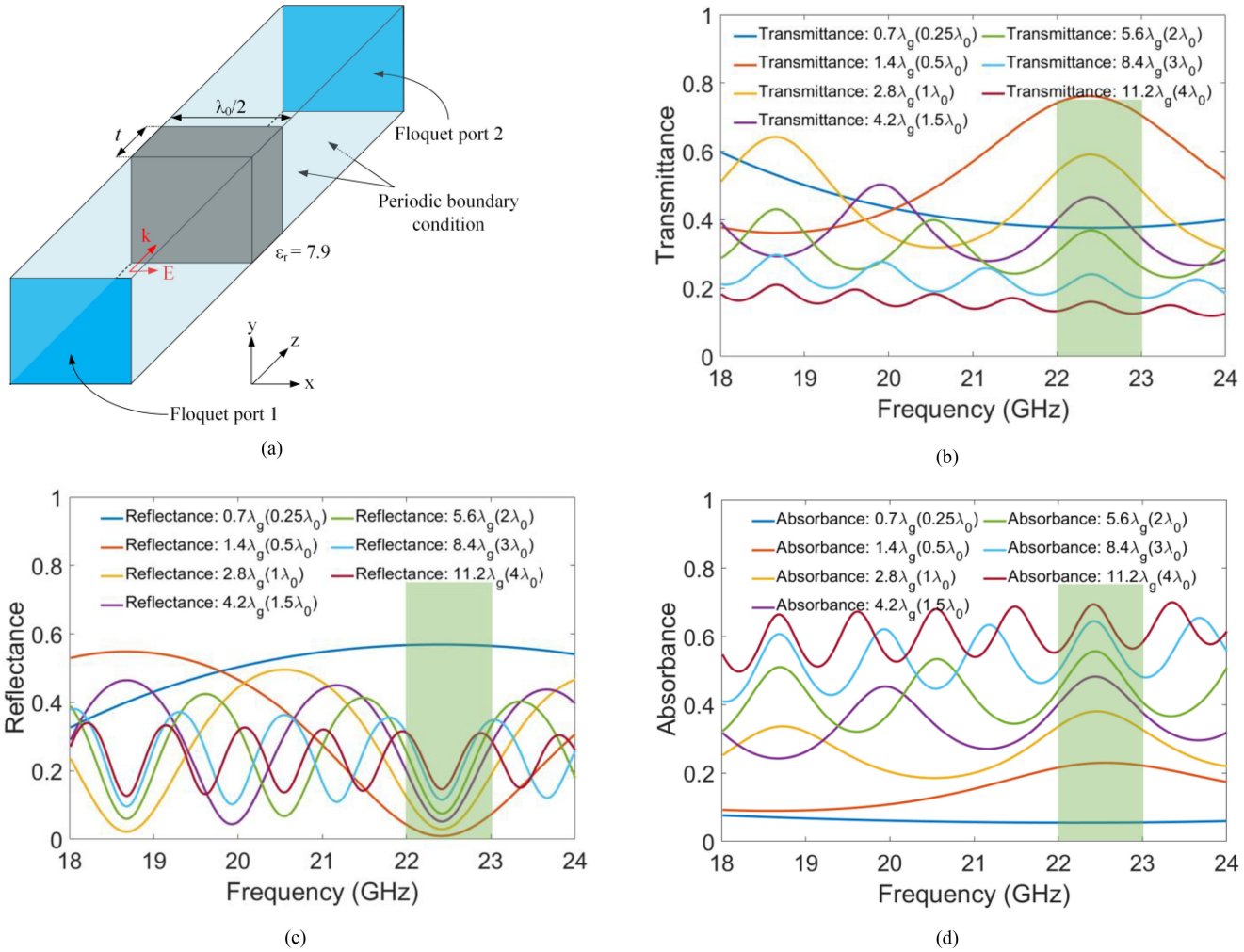


**FIGURE 1.** (a) Full-wave simulation setup of a wall's unit cell in CST Microwave Studio, (b) transmittance, (c) reflectance, and (d) absorbance at K-band frequencies for normal incidence under different thickness of the wall. Frequency selective window is highlighted.

operation in which the thickness of the wall would correspond to multiples of $\lambda_g$, where $\lambda_g$ denotes the wavelength inside the wall structure at the centre frequency within the investigated frequency band of operation. When this condition is met, transmission through wall will peak at the corresponding frequency. From Fig. 1, the presence of two such sub-bands is evident: 18-19 GHz and 22-23 GHz. In this work, the sub-band (or frequency selective window) of 22–23 GHz is chosen as the ideal band for computational TWI. It should be noted here that, according to the power conservation rule, for the analyses presented in Fig. 1, transmittance + reflectance + absorbance = 1.

In a practical implementation of this scenario, we use two rectangular waveguide probes placed in front of the wall to investigate the response of the wall, as shown in Fig. 2(a). The probes are set at the same distance of $d$ to the surface of the wall. The wall has a width of $6\lambda_0$ at the centre frequency of the 22-23 GHz band and a thickness of $t$. Next, the backscattered signal is analyzed to present the reflectivity of the wall. As can be seen in Fig. 2(b), in the presence of the Terrace stone wall, a large amount of the power from Port 1 transmitting to the wall is reflected and transferred to Port 2 in most of the frequency range, except in the bands of 18–19 GHz and 22–23 GHz. Within the 18-19 GHz frequency band, the thickness of the wall is approximately $t = 2.5\lambda_g$ at the centre frequency. Performing a simple Smith Chart analysis, it is evident that impedance is repeated at every $0.5\lambda_g$ interval with the wall structure. In practice, this would suggest that, moving along the wall structure, if the thickness of the wall is $0.5\lambda_g$ (or multiples of it), it then becomes possible to consider the wall structure, in terms of its impedance response, collapsing onto an infinitely thin plane. Similarly, for the 22-23 GHz band, the thickness of the wall is approximately $t = 3\lambda_g$, which is also a multiple of $0.5\lambda_g$. As a result, in Fig. 2(b), at both 18-19 GHz and 22-23 GHz, we observe frequency selective windows, and this outcome is in good agreement with the plane-wave analysis presented in Fig. 1, where two transmission windows were identified between 18-19 GHz and 22-23 GHz. In this work, we choose the 22-23 GHz frequency band as the frequency selective window,

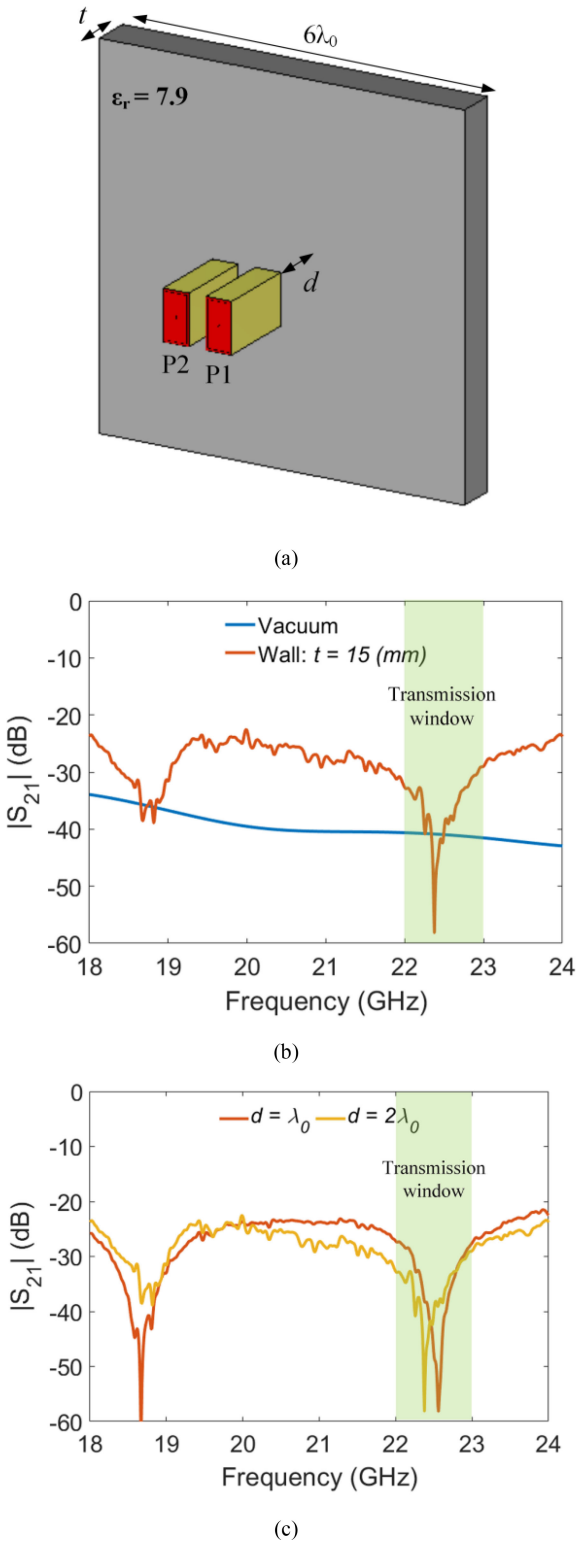


**FIGURE 2.** **(a) Full-wave model of the wall illuminated by two probes, (b) the backscattered signal levels from the wall (Terrace stone medium with $t = 15$ mm), and (c) the backscattered signal levels as a function of distance $d$ when the thickness of the wall is fixed to $t = 15$ mm. Frequency selective window is highlighted.**

corresponding to a transmission amount of greater than 55% and a reflection amount of below 5% when the wall thickness approaches $t = 3\lambda_g$ (see Fig. 1). Next, the backscattered signal levels are shown in Fig. 2(c) for different distances $d$ when the thickness of the wall is fixed. As can be seen in Fig. 2(c), when $d$ changes, the frequency-selective window within this band is not significantly affected, proving that the process of identifying the transmission window is reliable.

## III. DMA DESIGN FOR COMPUTATIONAL TWI

In this section, a two-port, 2D DMA consisting of an array of sparsely-distributed, tunable metamaterial elements is introduced for TWI in the identified frequency selective window. We leverage the capability of the DMA to operate over a narrow frequency bandwidth for TWI with no a-priori knowledge of the wall structure and characteristics. To this end, the 2D DMA developed in [38] will be used to evaluate the proposed method. In [38], the DMA operates in the 20-22 GHz frequency band to perform polarimetric computational imaging. In this work, the operating band of the DMA is extended to 22–23 GHz, which is one of the frequency-selective windows identified in Section II to achieve TWI. It should be noted here that once the transmission window is identified, the operating frequency of the DMA can be tuned electronically to match with the frequency of the transmission window. Albeit the DMA is required to operate across a narrow frequency band (i.e., transmission window), this narrowband imaging capability does not necessarily imply that the DMA cannot be tuned outside this window if the transmission window were to occur at another frequency when a different wall material is present.

Before discussing the TWI operation, we briefly demonstrate the structure of the DMA and refer to [38] for a more detailed analysis of the DMA architecture. As shown schematically in Fig. 3, the DMA consists of a parallel-plate waveguide structure with copper cladding on both sides and a via fence along the edges of the waveguide, creating a cavity. The front surface of the cavity is loaded with an array of two orthogonally oriented Jerusalem cross complementary electric-LC (JC-cELC) metamaterial elements. The metamaterial elements were designed to operate at K-band frequencies. This is achieved by populating the metasurface aperture with JC-cELC elements exhibiting slightly different resonant frequencies to cover the investigated frequency band of operation – similar to the metasurface concepts introduced in [14], [28]. The JC-cELC elements are distributed across the metasurface layer in a random fashion. Excitation of the metasurface is achieved using two coaxial probes located at $P_1$ and $P_2$ as shown in Fig. 3. Both ports launch a cylindrical wavefront inside the dielectric substrate bounded by the cavity boundaries. Upon reflection from the via fence, the field distribution inside the cavity is diverse (i.e., devoid of a regular pattern) and undergoes spatial variation as a function of frequency [14].

In addition to the frequency-diversity, the DMA aperture achieves an additional layer of spatio-temporal diversity due to the active modulation of the metamaterial elements across

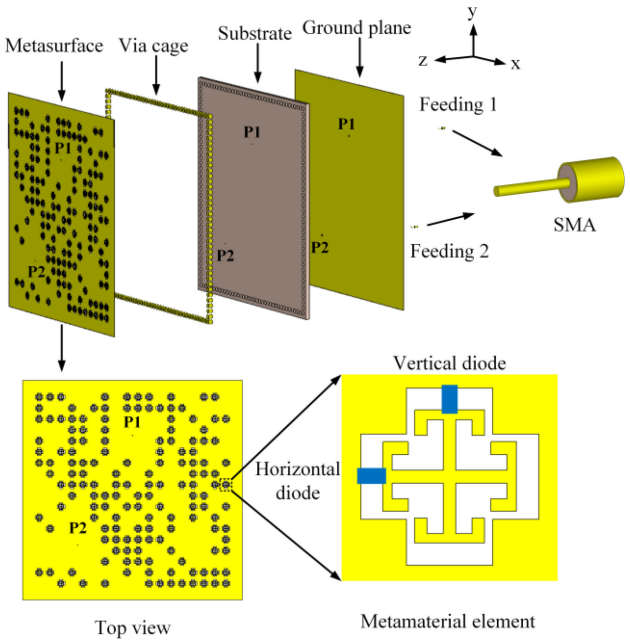


**FIGURE 3.** Configuration of the developed cavity-backed polarimetric DMA presented in [38].

the metasurface layer. In this implementation, each metamaterial JC-cELC element is loaded with two PIN diodes as depicted in Fig. 3. When the diodes are forward-biased, they effectively short-circuit the JC-cELC elements, ensuring that they cannot couple to the guided-mode inside the cavity, and hence, do not contribute to radiation in free-space. When the diodes are reverse-biased, the JC-cELC elements couple to the guided-mode at the intended frequency band, hence, contributing to radiation in free-space. As a result, when the frequency is fixed, the DMA can still radiate spatio-temporally varying field patterns by dynamically tuning the metamaterial elements across the metasurface layer *on* and *off* in a random fashion. In other words, at a single frequency, the interaction of the metamaterial elements with the guided-mode controls the amplitude and phase of the transmitted wave from the DMA aperture, such that spatio-temporally varying field patterns (or modes) can be generated by modifying the *on/off* states of the elements randomly along the aperture surface. It is important to emphasize here that both diodes are simultaneously switched *on* and *off* for a given JC-cELC element across the metasurface. Hence, the biasing of the unit cell structure can be achieved using a single DC terminal that is shared between the two diodes. Such a biasing structure can be realized using a radial-stub based network originally presented in [31].

The complex fields formed within the cavity project into the region to be imaged by superposing the contributions from each of the radiating metamaterial elements. In this DMA implementation, each configuration of the metasurface aperture (as it is dynamically tuned) is called a *mask*. These masks further allow for multiplexed backscatter measurements of a scene to be post-processed for imaging.

A significant advantage of the DMA-based computational TWI concept can be appreciated by considering the single-pixel physical layer compression offered by this architecture. The electrical size of the DMA is $8\lambda_0 \times 8\lambda_0$. A conventional, raster-scan based imaging modality would require this aperture to be sampled at the Nyquist limit ($\lambda_0/2$), suggesting that, conventionally, 17 x 17 individual antenna elements are needed to synthesize an aperture of this size. Facilitating the computational TWI concept with the DMA, however, only a single aperture with one transmit and one receive channel is used to synthesize the same aperture size.

In the design phase of the DMA aperture for computational TWI, the scattering parameters (or S-parameters) play an important role. Firstly, the DMA is required to exhibit a good impedance match to ensure that the exciting signal feeding the DMA is accepted with minimal reflection within the identified transmission window for imaging. Secondly, to ensure that the weak scattering from the imaged object behind the wall is not dominated by the cross coupling between the feeding ports of the DMA, this coupling level should be reasonably low. In Fig. 4, the simulated reflection coefficient and cross coupling patterns of the DMA are shown in free-space (i.e., in the absence of the wall structure and the imaged object). For this analysis, we have chosen four different mask configurations for brevity, but a similar analysis can be performed for a different number of masks without loss of generality. Analyzing Fig. 4(a), it is evident that the reflection coefficients of the DMA at the feeding ports remain around or below $-10$ dB across the selected frequency band of 22-23 GHz, ensuring that signals from both ports can transmit and receive efficiently. Similarly, in Fig. 4(b), the coupling level between the ports of the DMA is around or below $-10$ dB throughout the selected transmission window.

For the analyses presented in Fig. 4, it should be noted that the S-parameter optimization of the DMA does not have a unique solution. This is because, every time the DMA mask configuration is modulated (i.e., varying masks), the distribution of the radiating and non-radiating JC-cELC elements across the metasurface layer varies on a quasi-random basis. This, in turn, effectively, changes the boundary condition with which the guided-mode interacts at the metasurface layer. In other words, the guided-mode pattern inside the dielectric substrate is dependent on the metasurface mask configuration. As an example, one can appreciate that, feeding the antenna from the first port, when mask 4 is used, the $S_{11}$ pattern is around or below the $-10$ dB level across the entire band (solid black line in Fig. 4(a)), whereas when mask 1 is used, we have certain bands where the $S_{11}$ level becomes closer to $-8$ dB at some frequencies (solid blue line in Fig. 4(a)). Moreover, as well as the boundary condition imposed by the corresponding metasurface mask configuration, the impedance match is also a function of the location of the feeding port determining where the guided-mode is launched inside the dielectric substrate. As an example, it can be seen in Fig. 4(a) that, when the DMA is fed through port

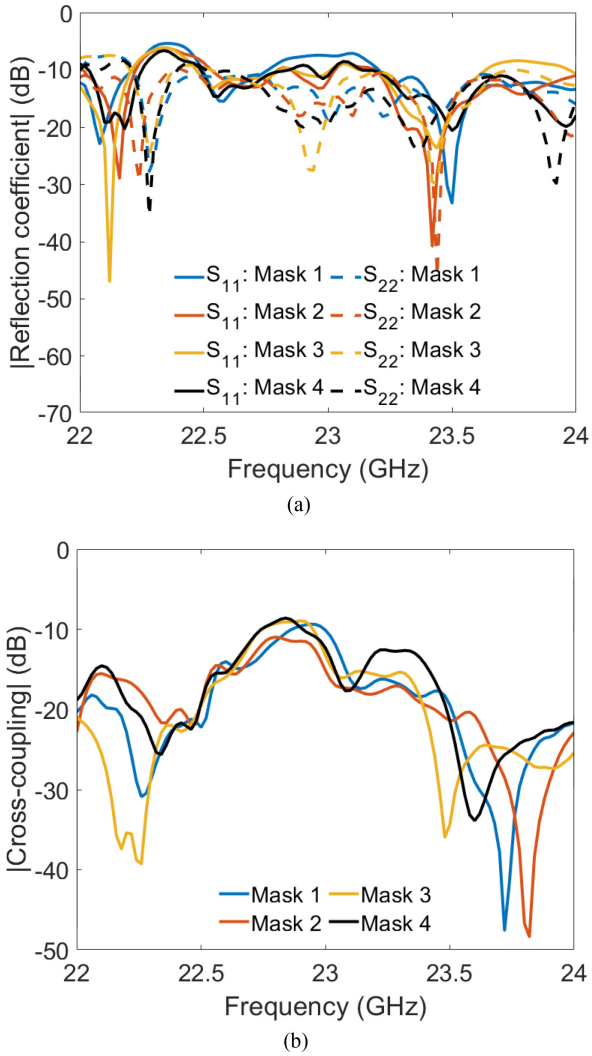


**FIGURE 4.** Simulated (a) reflection coefficient at each feeding port, and (b) cross-coupling between the feeding ports of the DMA.

2, the $S_{22}$ patterns are below the −10 dB level throughout the investigated frequency band for mask 2 and 4 configurations (dashed red and black lines in Fig. 4(a)). A similar outcome can also be observed for the cross-coupling patterns presented in Fig. 4(b). Analyzing Fig. 4(b), the dependency of the cross-coupling levels on the mask configuration is evident. As an example, for mask configurations 1 and 2, the cross-coupling level between the feeding ports remains below −10 dB for the entire investigated frequency band, whereas, for masks 3 and 4, the −10 dB value is slightly exceeded closer to 23 GHz. As a result, we use the term "around −10 dB" to accommodate slight variations above the −10 dB level. It is worth noting here that whereas the S-parameter analyses of the DMA between 22–23 GHz are presented in Fig. 4, the S-parameters of the DMA between 20–22 GHz were validated in [38]. This is important, because, in the next section, we will carry out computational TWI studies at both these frequency bands and provide a comparison between the reconstructed images to highlight the importance of operating within the transmission window.

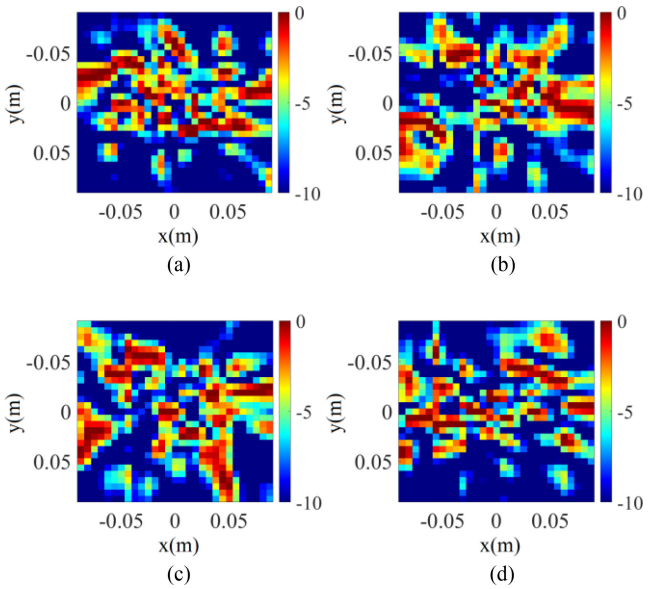


**FIGURE 5.** Simulated near-field patterns of the electric-fields radiated from the DMA with (a) mask 1, (b) mask 2, (c) mask 3, and (d) mask 4 at 22.5 GHz when exciting port 1. Colorbar: dB.

Another critical aspect in the design of the DMA aperture is the diversity of the field patterns radiated by the DMA [38]. In Fig. 5, we present the electric near-field patterns of the DMA aperture for four different mask configurations. Analyzing this figure, the diversity in the DMA radiated field patterns achieved as a function of varying masks can be appreciated. This is a key component for the quasi-random operation to encode the radar measurements using the DMA structure of Fig. 3. An increased diversity in the radiated field patterns from the DMA corresponds to an increased orthogonality between the measurement modes – a key aspect in reducing the information redundancy in the measurements collected by the DMA. The DMA concept eliminates the conventional raster-scan requirement because of the diverse field patterns that it generates, such as the ones presented in Fig. 5. This, effectively, eliminates the need for conventional, multi-pixel, raster-scan based transceiver architectures for imaging.

## IV. COMPUTATIONAL TWI

### A. THEORY OF COMPUTATIONAL IMAGING

The computational imaging process was outlined in detail in [28]. First, using the first Born approximation, a sensing matrix, $\mathbf{H}$, proportional to the antenna radiated fields, $\mathbf{H} \propto \mathbf{E}_{\mathrm{Tx}}\mathbf{E}_{\mathrm{Rx}}$, is computed. Here, $\mathbf{E}_{\mathrm{Tx}}$ and $\mathbf{E}_{\mathrm{Rx}}$ denote the fields radiated by the transmit and receive apertures propagated to the imaged scene domain. Next, the backscattered radar measurement vector, $\mathbf{g}$, is captured at the receiver. The relation between $\mathbf{g}$, $\mathbf{H}$ and the scene reflectivity, $\mathbf{f}$, is as follows:

$$\mathbf{g}_{\mathrm{M}\times 1} = \mathbf{H}_{\mathrm{M}\times \mathrm{N}}\mathbf{f}_{\mathrm{N}\times 1} + \mathbf{n}_{\mathrm{M}\times 1} \tag{1}$$

where $\mathbf{n}$ is the measurement noise. Here, the scene reflectivity, $\mathbf{f}$, can be estimated by means of several computational

reconstruction algorithms, such as pseudo-inverse, matched-filter, least-squares, and TwIST+TV [29]. To have a realistic imaging environment, the signal-to-noise ratio (SNR) for the imaging scenarios studied in this paper is 20 dB. The noise is added to the measurement vector as a Gaussian distribution with zero mean and variance of $\sigma^2 = SNR|g|$ [29]. Here, $|g|$ denotes the average received signal over all frequencies and masks.

It should be noted that, in Eq. (1), we use the bold font only to denote the vector-matrix notation while the fields forming the sensing matrix are scalar. In Eq. (1), $M$ denotes the number of total measurement modes radiated by the DMA to sample the scene information whereas $N$ is the number of pixels into which the imaged scene is discretized. Because the sensing matrix is not necessarily a square matrix, i.e., $M \neq N$, it does not have a direct inverse. In this work, the matched-filter technique is used for image reconstruction. Using matched-filtering, an estimate of the imaged scene can be reconstructed as follows:

$$\mathbf{f}_{est} = \mathbf{H}^{\dagger}\mathbf{g} \tag{2}$$

where the symbol $.^{\dagger}$ denotes the Hermitian transpose operator.

### B. IMAGING PERFORMANCE

In this section, we focus on demonstrating the capability of the developed DMA to achieve computational TWI over a narrow operating bandwidth with no a-priori knowledge of the wall structure. Additionally, a comparison between the images reconstructed in the frequency range of 20–22 GHz and 22–23 GHz is also provided. This comparison is of key importance for the presented technique because whereas our analyses in Figs. 1 and 2 show that the 22-23 GHz band exhibits a transmission window, the 20-22 GHz band is dominated by the strong reflections from the wall. To demonstrate computational TWI, using the DMA aperture, we image two different objects, an L-shaped object and a T-shaped object, located behind a wall. In imaging these objects, we discretize the selected frequency band of operation into $N_f = 51$ frequency points, and at each frequency, the aperture of the DMA is reconfigured to synthesize 15 mask configurations.

Fig. 6(a) shows the TWI configuration for the L-shaped object rotated by 45° imaged using the DMA. For this study, we demonstrate the extraction of target reflectivity, $\mathbf{f}_{est}$, in Eq. (2) using the numerical, full-wave simulated backscatter measurements of the imaged object in CST Microwave Studio. For this simulation, the wall is placed at $z = 80$ mm from the aperture surface in the near-field region. Then, the conductive target is placed behind the wall at $z = 5$ mm from the wall surface. The reconstructed image, $\mathbf{f}_{est}$, of the L-shaped phantom is shown in Fig. 6(b) for 22–23 GHz and in Fig. 6(c) for 20–22 GHz.

Analyzing the reconstructed image in Fig. 6(b), it can be observed that both diagonal strips of the L-shaped phantom exhibit a similar signature with equal amplitudes. For comparison, an outline of the imaged phantom is plotted on

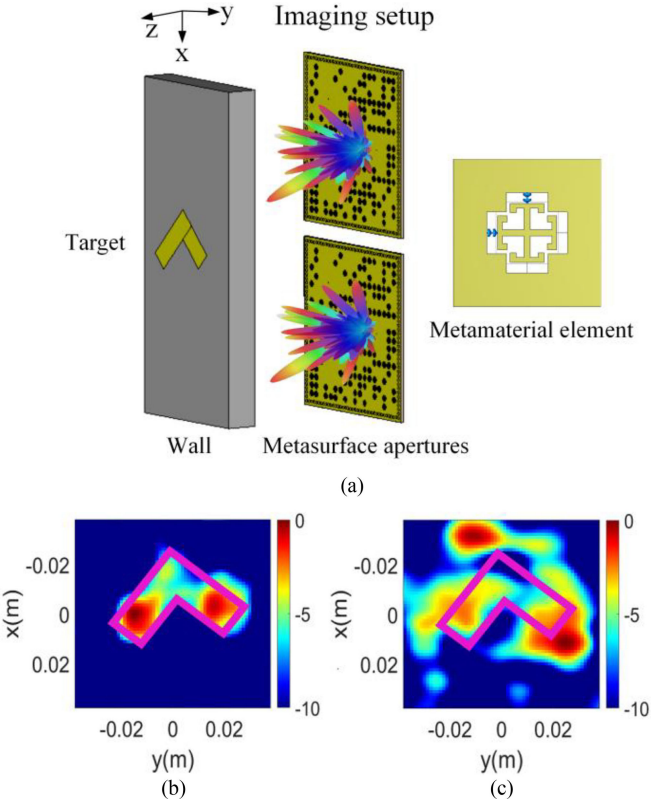


**FIGURE 6.** TWI of the L-shaped phantom rotated by 45°: (a) imaging setup in CST using the DMA with an example diverse radiation pattern plotted on top, (b) reconstructed image in 22-23 GHz with the outline of the imaged object plotted on top, and (c) reconstructed image in 20-22 GHz with the outline of the imaged object plotted on top. Colorbar: dB.

top of the reconstructed image. From Fig. 6(b), it is evident that, when the DMA is activated within the selected transmission window (22-23 GHz), the reconstructed image of the L-shaped object is in line with the actual outline of the object. On the contrary, when TWI is carried out within the 20-22 GHz band (i.e., outside the transmission window), the reconstructed image is significantly distorted. From this study, it can be concluded that the reconstruction of the L-shaped object produces a higher fidelity image when computational TWI is performed in the frequency range of 22–23 GHz, that is, the frequency selective window, so that the effect of the wall in the backscattered signal is minimized. In other words, the rather significant difference between the two cases is because the effect of the wall in the frequency range of 22-23 GHz is minimized whereas the backscattered signal in the frequency range of 20-22 GHz is dominated by the contribution from the wall.

In the presented computational TWI technique, once the transmission window is identified, the DMA aperture is activated to facilitate computational TWI within the selected frequency band. This, effectively, constitutes a sensor fusion scheme working in a successive fashion. It is worth mentioning here that the reconstruction fidelity in Fig. 6(b) can be further increased by increasing the number

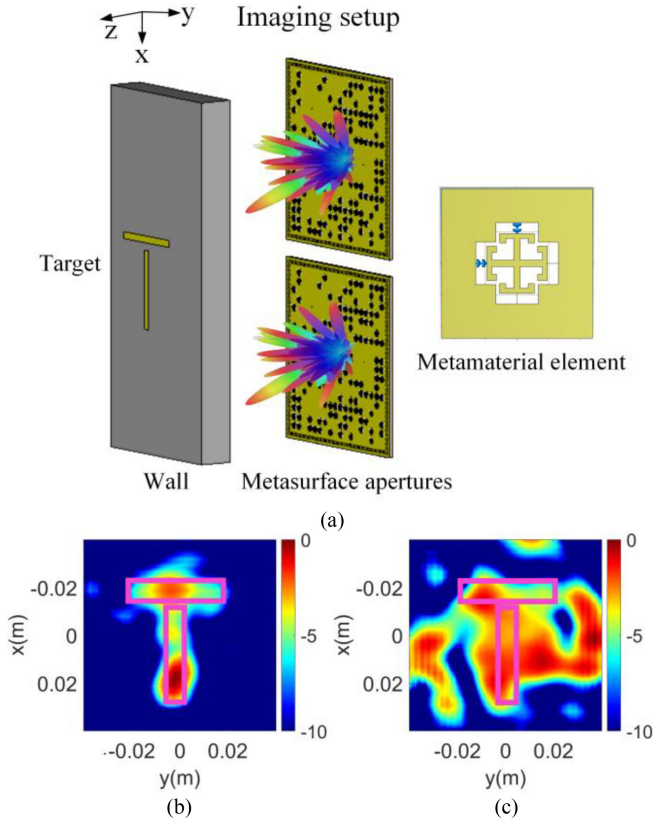


**FIGURE 7.** TWI of the T-shaped phantom: (a) imaging setup in CST using the DMA with an example diverse radiation pattern plotted on top, (b) reconstructed image in 22-23 GHz with the outline of the imaged object plotted on top, and (c) reconstructed image in 20-22 GHz with the outline of the imaged object plotted on top. Colorbar: dB.

of masks and using a larger aperture. However, increasing these parameters would also result in a significantly increased computational complexity for the full-wave simulations. Thus, rather than further improving the quality of the reconstructed images, we focus on the relative comparison between the reconstructed images when the DMA is activated within the identified transmission window and outside of the transmission window.

Following the imaging of the L-shape phantom, we next image the T-shaped object as depicted in Fig. 7. The object is located behind the same wall structure. Similar to the computational TWI study in Fig. 6, for this scenario, the DMA apertures are tuned to operate at two different frequency bands: 22-23 GHz (transmission window) and 20-22 GHz (outside the transmission window). The reconstructed images are shown in Figs. 7(b) and (c).

Analyzing the reconstructed images in Fig. 7, it is evident that leveraging the DMAs within the identified transmission window (22-23 GHz) helps significantly with eliminating the contribution of the wall response in the backscattered data, and hence, in the reconstructed image. On the contrary, by imaging within the 20-22 GHz frequency band, the reconstructed image of the T-shaped object is significantly distorted by the wall reflections.

## V. CONCLUSION

In this paper, we presented a sensor fusion scheme to achieve a computational TWI technique at microwave frequencies. This technique consists of a two-stage process. First, two probes are used to evaluate the EM characteristics of the wall, and an ideal transmission frequency band, called frequency selective window, is identified. Second, a DMA is leveraged to achieve TWI of an object within the selected frequency band. The DMA aperture is essentially a single-pixel microwave camera, eliminating the need for a raster-scan based approach to sample the scene information. The DMA concept achieves this by radiating diverse (or spatio-temporally varying) field patterns and encoding the backscattered scene information onto these measurements. Using this concept, the scene information is compressed into a single receiver channel per DMA. We showed that, by identifying an ideal transmission frequency band and limiting the operation frequency of the DMA to this band, TWI can be achieved without the need for a-priori knowledge of the wall characteristics. The obtained full-wave results confirm the feasibility of such a sensor fusion scheme to facilitate computational imaging for TWI, and potentially, other applications involving imaging through dielectric media.

## REFERENCES

[1] F. Soldovieri, R. Solimene, A. Brancaccio, and R. Pierri, "Localization of the interfaces of a slab hidden behind a wall," *IEEE Trans. Geosci. Remote Sens.*, vol. 45, no. 8, pp. 2471–2482, Aug. 2007.

[2] F. Ahmad, M. G. Amin, and S. A. Kassam, "Synthetic aperture beamformer for imaging through a dielectric wall," *IEEE Trans. Aerosp. Electron. Syst.*, vol. 41, no. 1, pp. 271–283, Jan. 2005.

[3] G. Gennarelli, G. Vivone, P. Braca, F. Soldovieri, and M. G. Amin, "Multiple extended target tracking for through-wall radars," *IEEE Trans. Geosci. Remote Sens.*, vol. 53, no. 12, pp. 6482–6494, Dec. 2015.

[4] B. Yektakhah and K. Sarabandi, "All-directions through-the-wall imaging using a small number of moving omnidirectional bi-static FMCW transceivers," *IEEE Trans. Geosci. Remote Sens.*, vol. 57, no. 5, pp. 2618–2627, May 2019.

[5] F. Ahmad, Y. Zhang, and M. G. Amin, "Three-dimensional wideband beamforming for imaging through a single wall," *IEEE Geosci. Remote Sens. Lett.*, vol. 5, no. 2, pp. 176–179, Apr. 2008.

[6] R. Solimene, F. Soldovieri, G. Prisco, and R. Pierri, "Three-dimensional through-wall imaging under ambiguous wall parameters," *IEEE Trans. Geosci. Remote Sens.*, vol. 47, no. 5, pp. 1310–1317, May 2009.

[7] J. Hunt *et al.*, "Metamaterial apertures for computational imaging," *Science*, vol. 339, no. 6117, pp. 310–313, 2013.

[8] J. Hunt *et al.*, "Metamaterial microwave holographic imaging system," *J. Opt. Soc. Amer. A Opt. Image Sci. Vis.*, vol. 31, no. 10, pp. 2109–2119, 2014.

[9] G. Lipworth *et al.*, "Metamaterial apertures for coherent computational imaging on the physical layer," *J. Opt. Soc. Amer. A*, vol. 30, no. 8, pp. 1603–1612, 2013.

[10] J. A. Martinez-Lorenzo, F. Quivira, and C. M. Rappaport, "SAR imaging of suicide combers wearing concealed explosive threats," *Progr. Electromagn. Res.*, vol. 125, pp. 255–272, Jan. 2012.

[11] J. Laviada, A. Arboleya-Arboleya, Y. Alvarez-Lopez, C. Garcia-Gonzalez, and F. Las-Heras, "Phaseless synthetic aperture radar with efficient sampling for broadband near-field imaging: Theory and validation," *IEEE Trans. Antennas Propag.*, vol. 63, no. 2, pp. 573–584, Feb. 2015.

[12] G. L. Charvat, L. C. Kempel, E. J. Rothwell, and C. M. Coleman, "An ultrawideband (UWB) switched-antenna-array radar imaging system," in *Proc. IEEE Int. Symp. Phased Array Syst. Technol.*, 2010, pp. 543–550.

[13] S. Withington, G. Saklatvala, and M. P. Hobson, "Partially coherent analysis of imaging and interferometric phased arrays: Noise, correlations, and fluctuations," *J. Opt. Socirty America A*, vol. 23, no. 6, pp. 1340–1348, 2006.
[14] M. F. Imani *et al.*, "Review of metasurface antennas for computational microwave imaging," *IEEE Trans. Antennas Propag.*, vol. 68, no. 3, pp. 1860–1875, Mar. 2020.
[15] J. N. Gollub *et al.*, "Large metasurface aperture for millimeter wave computational imaging at the human-scale," *Sci. Rep.*, vol. 7, Feb. 2017, Art. no. 42650.
[16] T. Fromenteze, C. Decroze, S. Abid, and O. Yurduseven, "Sparsity-driven reconstruction technique for microwave/millimeter-wave computational imaging," *Sensors*, vol. 18, no. 5, p. 1536, 2018.
[17] A. C. T. Yoya, B. Fuchs, C. Leconte, and M. Davy, "A reconfigurable chaotic cavity with fluorescent lamps for microwave computational imaging," *Progr. Electromagn. Res.*, vol. 165, pp. 1–12, May 2019.
[18] A. V. Diebold, M. F. Imani, T. Sleasman, and D. R. Smith, "Phaseless computational ghost imaging at microwave frequencies," *Appl. Opt.*, vol. 57, no. 9, pp. 2142–2149, 2018.
[19] R. Obermeier and J. A. Martinez-Lorenzo, "Sensing matrix design via mutual coherence minimization for electromagnetic compressive imaging applications," *IEEE Trans. Comput. Imag.*, vol. 3, no. 2, pp. 217–229, Jun. 2017.
[20] O. Yurduseven, J. N. Gollub, A. Rose, D. L. Marks, and D. R. Smith, "Design and simulation of a frequency-diverse aperture for imaging of human-scale targets," *IEEE Access*, vol. 4, pp. 5436–5451, 2016.
[21] T. Fromenteze *et al.*, "Computational imaging using a mode-mixing cavity at microwave frequencies," *Appl. Phys. Lett.*, vol. 106, no. 19, 2015, Art. no. 194104.
[22] O. Yurduseven *et al.*, "Computational microwave imaging using 3D printed conductive polymer frequency-diverse metasurface antennas," *IET Microw. Antennas Propag.*, vol. 11, no. 14, pp. 1962–1969, 2017.
[23] O. Yurduseven, T. Fromenteze, D. L. Marks, J. N. Gollub, and D. R. Smith, "Frequency-diverse computational microwave phaseless imaging," *IEEE Antennas Wireless Propag. Lett.*, vol. 16, pp. 2808–2811, 2017.
[24] Z. Wu, L. Zhang, H. Liu, and N. Kou, "Range decoupling algorithm for accelerating metamaterial apertures-based computational imaging," *IEEE Sensors J.*, vol. 18, no. 9, pp. 3619–3631, May 2018.
[25] O. Yurduseven, V. R. Gowda, J. N. Gollub, and D. R. Smith, "Printed aperiodic cavity for computational and microwave imaging," *IEEE Microw. Wireless Compon. Lett.*, vol. 26, no. 5, pp. 367–369, May 2016.
[26] O. Yurduseven, J. N. Gollub, K. P. Trofatter, D. L. Marks, A. Rose, and D. R. Smith, "Software calibration of a frequency-diverse, multistatic, computational imaging System," *IEEE Access*, vol. 4, pp. 2488–2497, 2016.
[27] R. Zhu, T. Zvolensky, and D. Marks, "Millimeter wave computational imaging with 3D printed leaky wave frequency diverse antenna," in *Proc. 41st Int. Conf. Infrared Millimeter Terahertz Waves (IRMMW-THz)*, Copenhagen, Denmark, 2016, p. 1.
[28] G. Lipworth *et al.*, "Comprehensive simulation platform for a metamaterial imaging system," *Appl. Opt.*, vol. 54, no. 31, pp. 9343–9353, Nov. 2015.
[29] O. Yurduseven *et al.*, "Resolution of the frequency diverse metamaterial aperture imager," *Prog. Electromagn. Res.*, vol. 150, pp. 97–107, Jan. 2015.
[30] T. V. Hoang *et al.*, "Spatial diversity improvement in frequency-diverse computational imaging with a multi-port antenna," *Results Phys.*, vol. 22, Mar. 2021, Art. no. 103906.
[31] T. Sleasman *et al.*, "Waveguide-fed tunable metamaterial element for dynamic apertures," *IEEE Antennas Wireless Propag. Lett.*, vol. 15, pp. 606–609, 2016.
[32] T. Sleasman, M. F. Imani, J. N. Gollub, and D. R. Smith, "Dynamic metamaterial aperture for microwave imaging," *Appl. Phys. Lett.*, vol. 107, no. 20, 2015, Art. no. 204104.
[33] T. Sleasman, M. Boyarsky, M. Imani, J. Gollub, and D. R. Smith, "Design considerations for a dynamic metamaterial aperture for computational imaging at microwave frequencies," *J. Opt. Soc. America B*, vol. 33, no. 6, pp. 1098–1111, 2016.
[34] A. V. Diebold, M. F. Imani, T. Fromenteze, D. L. Marks, and D. R. Smith, "Passive microwave spectral imaging with dynamic metasurface apertures," *Optica*, vol. 7, no. 5, pp. 527–536, 2020.
[35] M. F. Imani, T. Sleasman, and D. R. Smith, "Two-dimensional dynamic metasurface apertures for computational microwave imaging," *IEEE Antennas Wireless Propag. Lett.*, vol. 17, no. 12, pp. 2299–2303, Dec. 2018.
[36] T. A. Sleasman, M. F. Imani, A. V. Diebold, M. Boyarsky, K. P. Trofatter, and D. R. Smith, "Implementation and characterization of a two-dimensional printed circuit dynamic metasurface aperture for computational microwave imaging," *IEEE Trans. Antennas Propag.*, vol. 69, no. 4, pp. 2151–2164, Apr. 2021.
[37] T. Sleasman, M. F. Imani, M. Boyarsky, K. P. Trofatter and D. R. Smith, "Computational through-wall imaging using a dynamic metasurface antenna," *OSA Continuum*, vol. 2, no. 12, pp. 3499–3513, Dec. 2019.
[38] T. V. Hoang, V. Fusco, T. Fromenteze, and O. Yurduseven, "Computational polarimetric imaging using two-dimensional dynamic metasurface apertures," *IEEE Open J. Antennas Propag.*, vol. 2, pp. 488–497, 2021.
[39] K. Jemai, T. Krner, A. Varone, and J.-F.Wagen, "Determination of the permittivity of building materials through WLAN measurements at 2.4 GHz," in *Proc. IEEE 16th Int. Symp. Pers. Indoor Mobile Radio Commun.*, 2005, pp. 589–593.

**THE VIET HOANG** received the B.S. degree in electronics and telecommunications engineering from the Hanoi University of Science and Technology, Vietnam, in 2011, and the M.S. and Ph.D. degrees in electronics and electrical engineering from Dongguk University in 2013 and 2017, respectively.

From 2017 to 2020, he was a Postdoctoral Researcher with Metamaterial Electronic Device Research Center, Hongik University, Seoul, South Korea, where his major research was to develop meta-structured antennas and meta-surface. He is currently a Research Fellow with the School of Electronics, Electrical Engineering and Computer Science, Queen's University Belfast, U.K. His research interests include the development of polarimetric active metasurface antennas for microwave and millimeter-wave imaging.

**RUPESH KUMAR** received the M.S. and Ph.D. degrees in electronics and communication engineering from Telecom Paris (ENST) in 2011 and 2014, respectively. He joined the School of Electronics, Electrical Engineering and Computer Science, Queen's University Belfast in 2021, where he is currently a Research Fellow with the Centre for Wireless Innovation. He has developed and designed radar systems for different applications, such as indoor positioning, health-monitoring, and wireless sensing. He has also developed and designed embedded RFID sensors for IoT applications. His current research interests include millimetre-wave imaging system design, dynamic frontend antenna aperture design and optimization using machine learning approaches, FMCW radar system design, and modeling of mmWave imaging system.

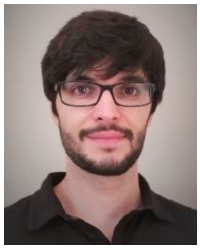

**THOMAS FROMENTEZE** received the Ph.D. degree from the University of Limoges, Limoges, France, in 2015. From 2015 to 2016, he was a Postdoctoral Researcher with Duke University, Durham, NC, USA. He is currently a Maître de Conférences (Assistant Professor) with the Xlim Research Institute, University of Limoges, Limoges, France. He is also an Adjunct Assistant Professor with the Center for Metamaterials and Integrated Plasmonics, Duke University. His research interests include ultra-wideband microwave and millimetre-wave imaging, wave propagation in complex media, computational/compressive imaging, and the various associated inverse problems. He has received the 11th EuRAD Young Engineer Prize during the European Microwave Week 2015.

**MARÍA GARCÍA-FERNÁNDEZ** was born in Luarca, Spain, in 1992. She received the M.Sc. and Ph.D. degrees in telecommunication engineering from the University of Oviedo, Spain, in 2016 and 2019, respectively. Since 2013, she has been involved in several research projects with the Signal Theory and Communications Research Group, TSC-UNIOVI, University of Oviedo. She was a visiting student with Stanford University, Palo Alto, CA, USA, from 2013 to 2014; a Visiting Scholar with the Gordon Center for Subsurface Sensing and Imaging Systems, Northeastern University, Boston, MA, USA, in 2018; and a Visiting Researcher with the Radar Department, TNO, The Hague, The Netherlands, in 2019. In 2022, she joined Queen's University Belfast as a Research Fellow with the Centre for Wireles Innovation. Her current research interests include inverse scattering, remote sensing, radar systems, imaging techniques, antenna measurement and diagnostics, and non-invasive measurement systems on board unmanned aerial vehicles. She was a recipient of the 2020 National Award to the Best Ph.D. Thesis on Telecommunication Engineering (category: telecommunications technologies and applications).

**GUILLERMO ÁLVAREZ-NARCIANDI** received the M.Sc. degree in telecommunication engineering and the Ph.D. degree from the University of Oviedo, Gijón, Spain, in 2016 and 2020, respectively. He was a visiting student with Stanford University, Stanford, CA, USA, in 2014; a Visiting Scholar with the University of Pisa, Italy, in 2018; and with the Institute of Electronics, Microelectronics and Nanotechnology, University of Lille, France, in 2019. In 2022, he joined Queen's University Belfast, as a Research Fellow with the Centre for Wireless Innovation. His research interests include radar systems and imaging techniques, antenna diagnosis and characterization systems, localization and attitude estimation systems, and RFID technology. He received the AMTA 2019 Student Paper Award (Second Place) and the Special Award to the Best Entrepreneurship Initiative in XV Arquímedes National Contest, in 2017, for the development of a RFID-based location system.

**VINCENT FUSCO** (Fellow, IEEE) specialises in microwave through sub-millimetre front-end circuit architectures. He has made seminal contributions to this field and holds a number of fundamental patents on self-tracking antennas and high performance micromachined frequency selective surfaces. He has published over 650 peer reviewed research papers, two books and holds 12 patents. In 2012, he was awarded the IET Senior Achievement Award the Mountbatten Medal and in 2019 the Royal Irish Academy Engineering Science Gold Medal. He is a member of the Royal Irish Academy and a Fellow of the U.K. Royal Academy of Engineering, the Irish Academy of Engineering as well as the Institution of Engineering Technology and is a Chartered Engineer.

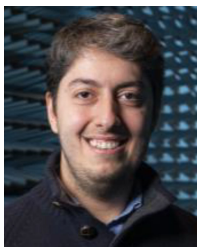

**OKAN YURDUSEVEN** (Senior Member, IEEE) received the B.Sc. and M.Sc. degrees in electrical engineering from Yildiz Technical University, Istanbul, Turkey, in 2009 and 2011, respectively, and the Ph.D. degree in electrical engineering from Northumbria University, Newcastle upon Tyne, U.K., in 2014.

He is currently a Senior Lecturer (Associate Professor) with the School of Electronics, Electrical Engineering and Computer Science, Queen's University Belfast, U.K. He is also an Adjunct Professor with Duke University, USA. From 2018 to 2019, he was a NASA Research Fellow with the Jet Propulsion Laboratory, California Institute of Technology, USA. From 2014 to 2018, he was a Postdoctoral Research Associate with Duke University. He has authored more than 150 peer-reviewed technical journal and conference articles and has been the Principal Investigator on research grants totaling in excess of £1.5M in these fields. His research interests include microwave and millimeter-wave imaging, multiple-input-multiple-output radars, wireless power transfer, antennas and propagation, and metamaterials.

Dr. Yurduseven was a recipient of several awards, including the Outstanding Postdoctoral at Duke University Award in 2017, the Duke University Professional Development Award in 2017, the NASA Postdoctoral Program Award in 2018, the British Council—Alliance Hubert Curien Award in 2019, the Leverhulme Trust Research Leadership Award in 2020 (£1M), the Young Scientist Award from the Electromagnetics Academy—Photonics and Electromagnetics Research Symposium in 2021, and the Queen's University Belfast Vice Chancellor's Early Career Researcher Prize in 2022. He has been serving as a Technical Program Committee Member in SPIE Defense and Commercial Sensing Conference since 2020 and a Guest Editor in several journals, including IEEE ANTENNAS AND WIRELESS PROPAGATION LETTERS, IEEE OPEN JOURNAL OF ANTENNAS AND PROPAGATION, and *Remote Sensing* (MDPI). He serves as an Associate Editor for the IEEE ANTENNAS AND WIRELESS PROPAGATION LETTERS and is a member of the European Association on Antennas and Propagation.